Crystal Chemistry and Thermodynamics of HREE (Er, Yb) Mixing in a Xenotime Solid Solution

Andrew C. Strzelecki[1,2,3,4], Margert Reece[1,2], Xiaodong Zhao[1,2,], Wendy Yu[1,2], Chris Benmore[5], Yang Ren[5,6], Christopher Alcorn[4], Artaches Migdisov[4], Hongwu Xu[4], Xiaofeng Guo[1,2,3,*]

[1] *Department of Chemistry, Washington State University, Pullman, Washington 99164, United States*

[2] *Alexandra Navrotsky Institute for Experimental Thermodynamics, Washington State University, Pullman, Washington 99164, United States*

[3] *Materials Science and Engineering, Washington State University, Pullman, Washington 99164, United States*

[4] *Earth and Environmental Sciences Division, Los Alamos National Laboratory, Los Alamos, New Mexico 87545, United States*

[5] *X-ray Science Division, Argonne National Laboratory, 9700 South Cass Avenue, Argonne, IL 60439, USA, Lemont, Illinois, 60439, UNITED STATES*

[6] *Department of Physics, City University of Hong Kong, Kowloon Hong Kong, China*

---

* e-mail: x.guo@wsu.edu

Abstract

Rare earth elements (REE), the thirteen naturally occurring lanthanides, yttrium, and scandium, are now ubiquitous in modern life as they are critical resources to many advanced technologies. However, the demand for the REEs is not equal, with the heavy rare earths (HREE) having a higher demand. Xenotime ($HREEPO_4$) is an important HREE ore mineral and globally is an economical source of HREE. Much of the crystallographic and thermodynamic properties of the xenotime end-members have been elucidated through a combination of calorimetric methods, solubility studies, and high-pressure studies. Yet, in natural systems, endmembers are rarely encountered, and instead, HREE solid solutions are more commonly observed. In this work, we report the crystal chemistry, thermodynamics of HREE mixing, and high temperature material behaviors and thermochemistry of a synthetic Er-Yb binary xenotime solid solution series ($Er_{(x)}Yb_{(1-x)}PO_4$), with implications for their mineralization processes and industrial applications as thermal coating materials. This was done through a combination of X-ray fluorescence spectrometry, synchrotron X-ray powder diffraction implemented with Rietveld analysis, Fourier transform infrared spectroscopy coupled with attenuated total reflectance, Raman spectroscopy, and thermogravimetric analysis coupled with differential scanning calorimetry.

1. Introduction

Rare earth elements (REE), the thirteen naturally occurring lanthanides, yttrium, and scandium,[1] are now ubiquitous in modern pedestrian life as they are critical resources to many advanced technologies. This is demonstrated by that REE are found utilized in the permanent magnets found in electric vehicles, wind turbines, and smartphones.[2] However, industrially, REE have been important commodities for over a hundred year, being utilized in everything from gas lighting mantels to petroleum cracking catalysis.[3] The list of potential applications for REE is ever-growing, with industries continually finding even more applications for the elements. The aerospace industry is an example that has historically used REE in guidance systems,[2] and now investigates many different types of REE-based ceramic materials to be as environmental barrier coatings (EBCs) in order to improve the efficiency of the combustion engines.[4–12] It is clear to predict that the demand for the REE will continue to surge, which, however, will certainly stress the overall supply of REE. While the REE have bulk crustal abundances equal to those of other industrially important metals such as copper, zinc, or molybdenum,[2,13] they are hardly ever concentrated to economic levels. REE are commonly subdivided into light (LREE) and heavy (HREE) based upon their atomic radii,[13,14] as the lanthanides exhibit a systematic decrease in atomic radii with increasing atomic number (Z).[15] The LREE consist of La – Eu and HREE consist of Gd– Lu, in addition to Sc and Y. Typically, the LREE comprise 60–90% of REE ores, whereas the HREE, which are in most industrial demand, are rarely concentrated to economic levels.[2,16,17] Up to date, there are only a few notable deposits (*i.e.* Lofdal (Namibia) and Browns Range (Australia)) where HREE can make up >80% of the total REE budget.[18–21]

In both of these deposits, xenotime ($HREEPO_4$) is an important ore mineral, and globally an economical source of HREE, which is commonly associated with other hydrothermal deposits.[22] Much of the thermodynamic properties on the xenotime end-members have been elucidated through a combination of calorimetric methods,[23–25] solubility studies,[22,26] and high pressure studies.[27–30] Albeit, in natural systems endmembers are seldomly observed, and instead, an intermediate composition, as a result of solid solutions, is more commonly presented. In solid solutions, the mixing behavior of the HREE in the xenotime structure ($I4_1/amd$) is paramount in modeling ore-forming processes.[31] If the HREE are mixing as ideal solutions, then no additional interaction parameter (W_x) is needed to model their thermodynamic behavior; however, if their

mixing is non-ideal, then regular solutions or subregular solutions will need to be employed, where W_x must be included in order to accurately describe their mixing behavior.[32] Although W_x of other REE phosphate minerals, monazite and cheralite, have been experimentally determined by calorimetric techniques,[33–35] only a few theoretical studies[36,37] and an empirically derived estimations[31] have been conducted on HREE xenotime.

As mentioned above, many REE-based ceramics materials are being investigated for a wide swath of applications as advanced ceramic material. The thermophysical and thermochemical properties of xenotime make it ideal to be used as EBC or thermal barrier coating (TBC) in aerospace applications[4] as the material possesses low chemical reactivity and a high melting point.[38–43] Currently, through the utilization of solid solutions, one can tailor and ultimately improve the thermophysical and thermochemical properties of EBC or TBC,[6] which is most likely a result of the entropy-driven stabilization effect.[44]

Additionally, the low chemical reactivity, low solubility, and resistance to radiation damage also make xenotime a promising ceramic waste host candidate for the permanent immobilization and disposal of actinides associated with nuclear waste.[45–50] As xenotime is isostructural to other zircon structure-type phases, including coffinite ($USiO_4$), thorite ($ThSiO_4$), and stetindite ($CeSiO_4$), they shares many similar thermochemical and thermophysical properties, while having the ability to accommodate trivalent elements, the dominate valence state of the late actinides (Am-Es).[51–53] As it has been found that actinides orthosilicates heavier than thorium are thermodynamically disfavored to form from their binary oxides,[54–56] the ability to have a ceramic waste host that allows the trivalent state is an obvious benefit. All of the actinide orthophosphates (Pu-Es) synthesized in the air have been reported to adopt the monazite structure,[49,51,57–60] yet there are also reports that Np and Pu were found to be stabilized in the xenotime structure ($Y_{(x)}An_{(1-x)}PO_4$, where An = Np or Pu) under reducing environments.[51] This stabilization within the xenotime structure could most likely be attributed to favorable energetics of mixing, similar to what is found with uranothorite ($Th_{(x)}U_{(1-x)}SiO_4$).[56,61,62]

Thus, studying the crystal chemistry associated with a xenotime solid solution series has both fundamental and applicable significance. In this work, we report the crystal chemistry, high temperature material behaviors, and thermodynamic stability of a Er-Yb binary xenotime solid solution series ($Er_{(x)}Yb_{(1-x)}PO_4$) with hydrothermal origins. This was done through a combination

of X-ray fluorescence (XRF) spectrometry, synchrotron X-ray powder diffraction implemented with both Rietveld, Fourier transform infrared spectroscopy coupled with attenuated total reflectance (FTIR-ATR), Raman spectroscopy, and thermogravimetric analysis coupled with differential scanning calorimetry (TGA-DSC).

2. Experimental Methods

2.1. Sample synthesis

$Er_{(x)}Yb_{(1-x)}PO_4$ were hydrothermally synthesized through modification of a method originally reported by Mesbah et al.,[63] for xenotime-thorite solid solutions. The following reagents were used: $Er(NO_3)_3{\cdot}5H_2O$, $Yb(NO_3)_3{\cdot}5H_2O$, H_3PO_4, $NaHCO_3$, NaOH, and HNO_3. The concentration of the solutions utilized was 0.05~0.3 M $Er(NO_3)_3{\cdot}5H_2O$, 0.05~0.3 M $Yb(NO_3)_3{\cdot}5H_2O$, and 0.05~0.3 M H_3PO_4. A 1.0 M solution of $NaHCO_3$ was prepared as a buffer and a 4~8 M NaOH solution and 8 M NaOH solution were used to adjust the pH to 8.7. The procedure involved pipetting stoichiometric amounts the Er^{3+}, Yb^{3+}, and PO_4^{3-} solutions into under constant stirring. The pH was then adjusted to 11 - 12 by dropwise addition of NaOH and subsequently buffered to 8.7 by adding $NaHCO_3$. The final solutions contained by a 23 mL Teflon line Parr autoclave were then placed in a pre-heated oven, of 220 ~ 250 °C for 7 days, followed by natural cooling to room temperature. The resulting precipitates were separated from the supernatant by centrifugation at 4000 rpm, washed 4-5 times with 18.2 mΩ deionized water and once with ethanol. The resulting solids were then dried overnight at 60 °C.

2.2. Total Reflection X-ray Fluorescence Spectroscopy (TXRF)

A Bruker S2 PICOFOX benchtop TXRF spectrometer equipped with an air-cooled molybdenum X-ray source 50 kV was used for the study.[64] The instrument's gain correction and resolution were calibrated prior to each series of measurements. Each measurement had an acquisition time of 120 secs and was performed in triplicate with the average reported here. The spectra were processed by Spectra 7 software using the optimized Bayes fit technique.[65] The resulting spectra are presented in Figures S1 and S2 and listed Table S1.

2.3. Thermogravimetric analysis coupled with differential scanning calorimetry (TGA-DSC)

The TGA-DSC measurements from 28 to 1200 °C, with a heating rate of 10°C/min, under a flowing N_2 atmosphere (20 mL/min), were performed by a Setaram SetSYS 2400 thermogravimetric differential scanning calorimeter. The temperature and sensitivity of the instrument were calibrated by heating indium, tin, lead, zinc, and aluminum across their fusion point repeatedly at the temperature change rates of 5, 10, 15, and 20 °C/min.

2.4. Vibrational Spectroscopies

Samples were characterized through a combination of FTIR and Raman spectroscopy. The FTIR spectra were recorded in the 600-4000 cm^{-1} range via a Perkin Elmer FTIR Spectrum 400 device. Powder samples were deposited directly on the surface of an ATR crystal without any prior preparation and with a collection time of 30 seconds and five scans. The Raman spectroscopic measurements were conducted using an HR Evolution Labram Raman Spectroscopy system equipped with both a 532 nm laser and a 785 nm laser to avoid the fluorescence of Er^{3+} (in the 532 nm laser) and Yb^{3+} (in 785nm). The laser outputs were filtered to 25-30 mW to prevent thermal damage. The total time of counting ranged from 3-120 seconds. The system is equipped with a grating of 600 gr/mm, which yields and effective resolution of less than $1cm^{-1}$. For both FTIR and Raman data, band component analysis was done by means of the Peakfit function within the OriginPro 2020 software suite using a Lorentz function with the minimum number of components. Correlation coefficient R^2 greater than 0.967 was obtained for all results displayed in Figures S5-S8 and reported within Tables S4-S6 and S8-S9.

2.5. Scanning Electron Microscopy & Energy Dispersive X-ray Spectroscopy (SEM-EDS)

Scanning electron microscopy was carried out to observe size distribution and surface morphology, by the FEI Apreo VolumeScopeTM SEM equipped with a field emission gun electron source, backscattered electron detectors, and TEAMTM Pegasus integrated EDS-EBSD. All micrographs were collected under high vacuum conditions with accelerating voltage of 20 kV, and magnifications from 50 times to 40,000 times. Images are deposited in the electronic supplement.

2.6. Synchrotron powder X-ray Diffraction (XRD)

Synchrotron powder X-ray diffraction was conducted at Sectors 6-ID-D and 11-ID-C of the Advanced Photon Source (APS) at Argonne National Laboratory (ANL). The wavelength of

the X-ray beam was 0.123696 Å (the distance to the detector between 350-360mm) and 0.1173 Å (1600 mm as the sample-detector distance), respectively, for 6-ID-D and 11-ID-C. All collected two-dimensional (2D) images were calibrated, masked, and integrated through the use of Dioptas processing software,[66] which were then analyzed through the Rietveld method using General Structure Analysis System software version II (GSAS-II),[68] where the instrument parameters were obtained using the CeO_2 standard. The backgrounds were modeled by the Chebyshev function with 6 - 20 coefficients.

3. Results

3.1. Thermogravimetric analysis coupled with differential scanning calorimetry (TGA-DSC)

TGA-DSC experiments (Figure 1) revealed that the samples have good thermal stability up to 1200 °C under an N_2 atmosphere. A long mass loss (~ 4.2 %) was identified from 50 to 1000 °C, which could correspond to the removal of absorbed and confined molecular water (in [001] channel of the xenotime structure), as well as hydroxyl species due to its endothermic nature. Such an attenuated or "sluggish" dehydration and dehydroxylation of other zircon-type materials have been previously reported and discussed in the works by Strzelecki and Barral et al.[67] Further details on the dehydration and dehydroxylation are discussed further in later sections. The samples recovered from the TGA-DSC experiments were further analyzed via synchrotron powder X-ray diffraction, FTIR-ATR, and Raman spectroscopy.

3.2. Synchrotron powder X-ray Diffraction (XRD)

The diffraction patterns of the pristine samples confirmed single-phased orthophosphate ($I4_1/amd$), with no observed impurities or chemical inhomogeneities (Figure S3). We performed the Rietveld refinements based on the structural models reported by Ni et al.[69] for $ErPO_4$ and $YbPO_4$. The occupancy of the MO_8 site in $Er_{(x)}Yb_{(1-x)}PO_4$ was fixed to the compositions determined by TXRF. The resulting refinements yielded R_{wp} values ranging from 2.65 to 8.34 %. The pristine xenotime phase is nanocrystalline, with a size ranging from 15 - 70 nm, typical of a synthetic hydrothermal route.[70–75] In the diffraction patterns of the samples recovered after the TGA-DSC to 1200 °C, there was additional diffraction peaks in each composition (Figure S4), not attributed to any reflection of xenotime, but to a Er-Yb sesquioxide solid solution phase ($Er_{(2x)}Yb_{(2-2x)}O_3$),

which is isostructural to bixbyite (*Ia*3).[76] As xenotime has been found to be thermally stable to over 1600 °C, which is its melting point,[38] the observations of $Er_{(2x)}Yb_{(2-2x)}O_3$ post-1200°C imply several possibilities. The first, and most likely, is that there was amorphous $Er_{(2x)}Yb_{(2-2x)}O_3$ in the sample, similar to what has been found in the hydrothermal synthesis of uranothorite.[77] The other reason is that the hydroxylated samples ($Er_{(x)}Yb_{(1-x)}PO_{4-x}OH_x$) thermally decompose to $Er_{(2x)}Yb_{(2-2x)}O_3$ and P_2O_5. As there are no observable reflections for P_2O_5, nor any exothermic signatures from DSC for thermal decomposition, this has been ruled out.

The refined unit cell parameters of $Er_{(x)}Yb_{(1-x)}PO_4$ are listed in Tables S2 and S3 and also in Figure 2. The unit cell parameters of the pristine and thermally treated $Er_{(x)}Yb_{(1-x)}PO_4$ decrease as a linear function of *x* following Vegard's law. However, both the unit cell volume and the *a*-axis of all sample compositions significantly decrease after being thermally treated to 1200 °C. Whereas the *c*-axis for some of the compositions was found to be increased for some compositions and decreased in others. Hypotheses for the cause of the change in unit cell parameters after the thermal treatment to 1200°C are discussed in the succeeding sections.

3.3. Vibrational Spectroscopies

The FTIR spectra were recorded for both the pristine samples (Figure 3a) and those after TGA-DSC to 1200 °C (Figure 3b). The spectra of the pristine samples could be separated into three distinct zones of interest: 600 – 1300 cm^{-1}, 1300 – 2000 cm^{-1}, and 2500 – 4000 cm^{-1}. The spectra of those collected after TGA-DSC to 1200 °C only had one distinct zone of interest being that of the first zone (600 – 1300 cm^{-1}). As xenotime is isostructural to zircon, it shares the same vibrational behavior that the band assignments reported in Nasdala et al.[81] and Dawson et al.[78] for zircon can be used to assign the internal vibrational modes of the PO_4 tetrahedron. The $I4_1/amd$ space group has seven active FTIR vibrational modes, which were determined again through a factor-group analysis.[78,79] These vibrational modes can be assigned to the internal and external vibrations of the PO_4 tetrahedron. Of the seven vibrational modes, four ($\Gamma_{int} = 2A_{2u} + 2_{Eu}$) can be assigned to internal vibrational modes and three ($\Gamma_{ext} = A_{2u} + 2_{Eu}$) can be assigned to external vibrational modes. The vibrations observed within 600 – 1300 cm^{-1} corresponds to the internal vibrational modes of the PO_4 tetrahedron. Noted that a wide massif was systematically recorded between 700 – 1200 cm^{-1}, similar to what was found in work by Clavier et al.,[80] which makes it difficult to unambiguously discriminate the components assigned to symmetric and antisymmetric

stretching vibrations. As only the antisymmetric internal motions of the PO_4 tetrahedron are visible by IR, due to symmetry reasons, this would mean that the doubly degenerate antisymmetric stretching mode ($\nu_3 - E_u$) is around 998 cm^{-1}, while the antisymmetric stretching mode ($\nu_3 - A_{2u}$) would be around 1125 cm^{-1}. The sharp band centered between 600 – 700 cm^{-1} corresponds to the antisymmetric deformation mode (ν_4 - A_{2u}) and occurs around 639 cm^{-1}. Then, the doubly degenerate antisymmetric deformation mode (ν_4 - E_u) and the three external vibrational modes ($\Gamma_{ext} = A_{2u} + 2_{Eu}$) were not able to be observed as they appear below 600 cm^{-1}.

The vibrational bands occurring in 1300 – 2000 cm^{-1} and 2500 – 4000 cm^{-1} are indicative of hydration and hydroxylation, which only appear in the pristine samples. Three relatively sharp vibration bands were observed, with the first corresponding to the deformation band of hydroxyl (OH^-) groups located near 1300 cm^{-1}, the second located near 1400 cm^{-1} for the stretching mode of CO_2, and the third near 1600 cm^{-1} for the deformation band of molecular water. Lastly, a large broad band in high wavenumbers (~3500 cm^{-1}) corresponds to the stretching modes of both hydroxy groups and molecular water.[82,83]

For Raman spectroscopy, the *I*4_1*/amd* space group has twelve active Raman vibrational modes, belonging to the D_{4h} point group.[78,79,84] Seven ($\Gamma_{int} = 2A_{1g} + 2B_{1g} + B_{2g} + 2E_g$)[78,84] can be assigned to the internal vibrations of the PO_4 tetrahedron, while the remaining five ($\Gamma_{int} = 2B_{1g} + 3E_g$)[78,84] can be assigned to the external vibrations of the PO_4 tetrahedrons.[78,84,85] Due to the interaction of the PO_4 tetrahedrons with the MO_8 dodecahedrons, the tetrahedrons cannot be considered as strictly independent units.[86] As a result of these interactions, there has yet to be a reporting of spectra with all twelve of the active Raman modes for materials of the zircon structure-type.[79]

All the spectra from the two lasers are separated into two distinct zones of interest (Figure 4): 900 – 1200 cm^{-1} and 100 – 900 cm^{-1}. First, P-O stretching motions are observed and assigned as the symmetric stretching (ν_1 - A_{1g}) occurring around 1005 cm^{-1}, the anti-symmetric stretching ($\nu_3 - B_{2g}$) occurring around 1065 cm^{-1}, and doubly degenerate anti-symmetric stretching (ν_3 - E_g) occurring around 1029 cm^{-1}. The second zone contains the internal bending motions of the PO_4 tetrahedron, and the lattice or external motions of the PO_4 tetrahedron. In addition, this zone is where the majority of Er^{3+} and Yb^{3+} fluorescence is observed when using the 532 and 785 nm laser, respectively. However, several of the bands were able to be assigned as the symmetric

bending (ν_2 - A_{1g}) occurring around 492 cm^{-1} and the anti-symmetric bending (ν_4 – B_{2g}) occurring around 692 cm^{-1}. The spectra and peak positions are in excellent agreement with previously reported by Begun et al.,[87] for $ErPO_4$ and $YbPO_4$.

4. Discussion

4.1. Role of hydration and hydroxylation on the xenotime structure

The mass losses observed in TGA from 50 to 1000 °C are interpreted to be a combination of the breakdown of hydroxylated phosphate tetrahedrons ($PO_{4-x}(OH)_x$), similar to what has been observed with zircon[82,88] and coffinite[67] and also the release of confined molecular water within the [001] channels in the xenotime structure, which has been confirmed for coffinite[89] and stetindite.[67] This is also supported by the determined unit cell parameters of samples after TGA-DSC in comparison to those of the pristine samples (Figure 2). First, the unit cell volume has a significant decrease (1.5% ± 0.2%) after being heated to 1200 °C, which agrees extremely well with those of the end-members previously reported by Ushakov et al.[25] and Ni et al.[69], who used flux-grown crystals that were completely anhydrous.

The reduction in the unit cell volume is mainly a result of the decrease in the *a*-axis. The [001] channels are perpendicular to the *a*-axis, and thus, control the dimensionality of the axis. This further collaborates with the original hypothesis of Janeczek[89] and those of Strzelecki & Barral et al.[67]. In work by Kijowska in 2003, the author also observed a prolonged mass loss via TGA-DSC and contractions of the unit cell parameters on the material recovered afterwards,[90] which, however, was hypothesized to be related to zeolitic water. In regard to the *c*-axis, there was no systematic trend before and after thermal treatments. This may be because of the cancellation of hydrated and hydroxylated features, the latter of which yields a shorter unit cell axis than one without.[67,88] The vibrational spectroscopy collaborates with all previous assertions. The FTIR spectra indicate that the pristine materials are clearly both hydrated and hydroxylated (Figures 3a, S7), whereas post-TGA samples are completely anhydrous. From Raman spectra, the positions of the ν_1 and ν_3 vibrational bands move to higher wavenumbers after being calcined (Figure 5), which indicates the decrease in P-O bond length upon calcination and implies the removal of the confined [001] water.[88] Again, this is in excellent agreement with observations by Strzelecki & Barral et

al.[67] on $CeSiO_4$, where the ν_1 and ν_3 vibrational bands shift to higher wavenumbers using *in situ* high temperature Raman spectroscopy.

4.2. Thermodynamics of Xenotime Solid Solutions with Implications for Their Mineralization

When looking at the size distribution of the ionic radii of the HREEs within the xenotime structure ($^{VIII}r_{HREE^{3+}}$), the average size is 1.008 Å, closest to that of Er^{3+} (1.004Å). The maximum difference in ionic radii exhibited by the HREEs in the xenotime structure is 6.25 % (Tb & Lu), while the average difference in the size of the ionic radii is 2.0 %, approximately that of Er^{3+} and Yb^{3+} (1.9 %). On the other hand, naturally occurring xenotime is dominated by Y^{3+}, which reflects that it has the highest overall geochemical abundance of any HREE.[91] The difference in size between Y^{3+} and other HREE is 1.8 %, also approximately that of Er^{3+} and Yb^{3+} (1.9 %). Therefore, the $ErPO_4$-$YbPO_4$ solid solution system is an ideal system in understanding the thermodynamic mixing behavior of HREE in the natural xenotime systems.

The results of the XRD (and Raman) indicate that the mixing of Er and Yb in $Er_{(x)}Yb_{(1-x)}PO_4$ follows Vegard's Law, as their unit cell parameters have a nearly linear dependency as a function of *x*. This would imply that a regular solution model should be employed effectively to evaluate the thermodynamics of cationic mixing in the $ErPO_4$-$YbPO_4$ solid solution. In accordance with the regular solution model, the Gibbs free energy of mixing can be calculated:

$$\Delta G_{mix} = \Delta H_{mix} - T\Delta S_{mix} \quad (1)$$

where both the enthalpy of mixing (ΔH_{mix}) and the entropy of mixing (ΔS_{mix}) are needed. As the regular solution model is being used, ΔH_{mix} can then be expressed by using the interaction parameter (W_x):

$$\Delta H_{mix} = W_x \cdot x \cdot (1 - x) \quad (2)$$

Typically, W_x is experimentally determined through calorimetric techniques,[56,92–97] or empirically approximated through a method employed by Migdisov et al.,[31] which requires the knowledge of unit cell volume and Young's modulus:

$$W_x = \overline{E}\left(\frac{\Delta V^2}{6V}\right) \quad (3)$$

where $\overline{E}$ is the average Young's modulus of all the REE xenotime end-members (168.8 GPa),[31] and ΔV is the difference between the molar volumes of the endmembers of interest. The average molar volumes of the thermally treated endmembers determined from data experimentally collected in this work is 42.453 ± 0.009 cm^3/mol for $ErPO_4$ and 41.646 ± 0.005 cm^3/mol for $YbPO_4$. Using these values, we determine the W_x for mixing Er and Yb in $ErPO_4$-$YbPO_4$ to be 0.44 ± 0.12 kJ/mol. Glynn[98] proposed that in order for a solid-solution system to be thermodynamically stable, the interaction parameter needs to be constrained by $W/(K_BT) < 2$, which then transforms to $W < 5$ kJ/mol under ambient conditions.[31,98] The newly derived value of W_x is well beneath this threshold and indicates that there should not be any miscibility gaps between $ErPO_4$ and $YbPO_4$. Furthermore, this derived value is in good agreement with the value predicted by Migdisov et al.[31] (0.36 kJ/mol). Using equation 2, we can then predict the enthalpy of mixing of the $ErPO_4$-$YbPO_4$ solid solution system (Figure 6a). As the value of W_x is slightly positive, the derived enthalpy of mixing is also weakly endothermic. This implies that the solid solution is enthalpically not favorable to form. While this conclusion builds upon the work done previously by Migdisov et al.[31] in confirming their empirical derivation for W_x, there is limitations to this value that the average Young's modulus of xenotimes was only estimated that has not yet to be measured and confirmed experimentally. Thus, the true value of W_x should be determined experimentally by other techniques, such as high temperature oxide melt drop solution calorimetry.

To effectively evaluate ΔS_{mix}, we calculated both configurational entropy of mixing ($\Delta S_{mix,config}$) and vibration entropy of mixing ($\Delta S°_{mix,vib}$) of Er^{3+} and Yb^{3+} in the MO_8 dodecahedron site at room temperature. Here the configurational term was calculated using the Boltzmann entropy formula:

$$\Delta S_{mix,config} = -R\cdot[(1-x)\cdot\ln(1-x) + x\cdot\ln(x)] \quad (4)$$

whereas the $\Delta S°_{mix,vib}$ was estimated by using an empirical relation of standard entropy of formation ($S°_{298\ K}$) to the molar volume (V_m) of a compound.[99,100] Typically, the linear equations presented in Jenkins and Glasser are used to calculate $S°_{298\ K}$.[44,101–103] However, large discrepancies between the experimentally derived values of $S°_{298\ K}$ for other phosphate minerals[22–24,104–106] was found when applying these equations. Therefore, we derived our own empirical relation of standard $S°_{298\ K}$ and V_m that minimizes the discrepancies between the experimentally derived

values of $S°_{298\ K}$ for phosphate minerals[22–24,104–106] (Figures S10 & S11). This empirical relation is represented in the following equation:

$$S°_{298\ K} = k\cdot(V_m) + c \qquad (5)$$

where the two correlation coefficients k is 2.46 ± 0.03 /J K^{-1} mol^{-1} and c is 5.79 ± 7.03 /J K^{-1} mol^{-1}, and V_m is the experimentally obtained molar volume (cm^3) of $Er_{(x)}Yb_{(1-x)}PO_4$. This value largely reflects the change in the vibrational entropy based on the volumetric change of the unit cell. The calculated $S°_{298\ K}$ for each of the $Er_{(x)}Yb_{(1-x)}PO_4$ compositions are presented in Table S9. By calculating the difference between $S°_{298\ K}$ of $Er_{(x)}Yb_{(1-x)}PO_4$ and endmembers ($ErPO_4$ and $YbPO_4$), an approximate $\Delta S°_{mix,vib}$ was extracted and combined with the configurational $\Delta S_{mix,config}$ to yield an estimate for ΔS_{mix} (Figure 6b). Using all this information, ΔG_{mix} at 25, 100, 250, and 400 °C were obtained and plotted in Figure 6c. These elevated temperatures were selected based on geochemical knowledge, such as fluid inclusion homogenization temperatures, reported for known REE deposits.[19,107–110]

While it was found that ΔH_{mix} was endothermic and thus thermodynamically unfavorable, the overall ΔG_{mix} was found to be exothermic. This implies that ΔS_{mix} is the driving force for the mixing of Er^{3+} and Yb^{3+} in the xenotime cationic sublattice. As stated earlier, the $ErPO_4$-$YbPO_4$ solid solution system is an ideal system in understanding the mixing behavior of HREE. This then further indicates that ΔS_{mix} is also the dominating driving factor for HREE mixing in xenotime. This result is reasonable because HREE have their 4f electrons more deeply shielded due to lanthanide contraction, and thus, their bonding are dominantly ionic. It is also interesting to compare this work (mixing of HREE in xenotime) to the mixing of early actinides in an isostructural system (mixing of Th and U in zircon), the latter of which shows a strong influence on the thermodynamics of mixing from ΔH_{mix} rather than ΔS_{mix}, originated from the relatively stronger covalent characters.[56,62] We then can conclude that mixing HREE in xenotime is ideal due to the pure ionicity, which may become non-ideal when early actinides and/or LREE are presented for mixing (*i.e.*, $HREE_{(x)}An_{(1-x)}PO_4$, where An = Th, U, Np or Pu).

4.3. High Temperature Thermochemistry of $Er_{(x)}Yb_{(1-x)}PO_4$

With interests in numerous fields of materials science in using $HREEPO_4$ in various high temperature applications, such as being used as a topcoat for EBC in the aerospace industry, it is necessary to understand the bulk thermochemistry of $HREEPO_4$ phases at high temperatures. Here we calculated the necessary remaining thermodynamic parameters of $Er_{(x)}Yb_{(1-x)}PO_4$ in order to evaluate the materials suitability under such environments. Firstly, it is paramount to have the heat capacity (C_p), the function of which will yield temperature-dependent enthalpy and entropy terms of a given phase:

$$\Delta H_T = \Delta H_{298} + \int_{298}^{T} C_p dT \qquad (6)$$

$$\Delta S_T = \Delta S_{298} + \int_{298}^{T} \frac{C_p}{T} dT \qquad (7)$$

Although C_p of both $ErPO_4$ and $YbPO_4$ have been determined experimentally by various calorimetric techniques,[24,26,41,42] C_p of the intermediate compositions, although not available, may be estimated by employing the Nuemann-Kopp's rule that relies on the summation of known C_p of its constituent binary oxides.[111] The derived C_p[104,112] were in good agreement with the previously reported data for each of the end-member phases (Figure S11).[24,26,41,42] ΔH_T and ΔS_T can then be calculated and combined to ΔG_T for each composition for the following potential reaction of interest to the aeronautical industry, $Er_xYb_{1-x}PO_{4(solid)} + 3H_2O_{(gas)} \rightarrow Er_xYb_{1-x}(OH)_{3(gas)} + H_3PO_{4(gas)}$. However, due to the lack of gas-phase thermodynamic data of H_3PO_4 at high temperatures, thermochemistry of the above reaction cannot be assessed. Therefore, we performed a thermochemical evaluation of just the $Er_{(x)}Yb_{(1-x)}PO_4$ solid solution phase up to 727 °C (or 1000 K), with their detailed thermodynamic parameters deposited in the electronic supplement. As temperature increases, the effects of the positive entropy of mixing become increasingly more obvious that at the highest temperature investigated (727°C), an overall deviation of the composition-dependent ΔG_f toward the exothermic direction began to emerge (Figure 7). The maximum of the negative curvature is at the composition where the concentration of Er is nearly equal to that of Yb. This implies that that the entropy of mixing in the $Er_{(x)}Yb_{(1-x)}PO_4$ solid solution is further enhancing the thermal stability with respect to the end-members.

Thus, from an application point of view, if $Er_{(x)}Yb_{(1-x)}PO_4$ is used as an EBC material, one should synthesize the material that realizes an equal molar of Er and Yb. Furthermore, in order to further increase the favorable entropy of mixing and ultimately improve the thermal stability,

multiple HREE in nearly equal molar quantities would be recommended. Ideally, the selected HREE should be chosen so that the differences are minimized for their ionic radii and thus the steric effect. For instance, mixing of equal molar portions of Y, Ho, Er, Tm, and Yb (the maximum difference in size is only 3.4%) will generate 14.4 J/mol·K (using equation 4) to benefit thermal stability that scales up with temperature. Recent work by Zhao et al. applied such a high-entropy concept to $LREEPO_4$-monazite with promising results.[113] The advantage of the $HREEPO_4$-xenotime system over the $LREEPO_4$-monazite system is that the predicted W_x of HREE is smaller than those for the LREE.[31] From a manufacturing and processes perspective, this would lead to more predictable phases being able to be produced, as there would be less likelihood for developing nanodomains or exsolution.[114] Overall, these observations and the subsequent discussion support the concept for high entropy oxides,[115] similar to their alloy counterparts that make the use of entropy of mixing to develop materials with superior high temperature stability.[116]

5. Conclusions

The crystal chemistry of a binary $ErPO_4$-$YbPO_4$ xenotime solid solution was explored through a combination of X-ray fluorescence (XRF) spectrometry, synchrotron X-ray powder diffraction implemented with Rietveld analysis, Fourier transform infrared spectroscopy coupled with attenuated total reflectance (FTIR-ATR), Raman spectroscopy, and thermogravimetric analysis coupled with differential scanning calorimetry (TGA-DSC). It was found that water has a profound role in the thermal stability of the xenotime phase, when prepared or originated hydrothermally. Furthermore, the unit cell parameters of the xenotime solid solution follow Vegard's law, strongly suggesting a random distribution of Er and Yb in the metal sites of xenotime. This further enables the complete thermodynamic analysis using a regular solution model, where the entropy of mixing is the dominating term that dictates the thermodynamic stability of $ErPO_4$-$YbPO_4$. It is expected that the use of HREE solid solution or high entropy xenotime ceramics as environmental barrier coating or thermal barrier coating will be greatly benefited by the entropy-driven stabilization.

Acknowledgements

This research was supported by the institutional funds from the Department of Chemistry at Washington State University (WSU). We also acknowledge the support by the U.S. Department of Energy (DOE), Office of Nuclear Energy, Grant No. DE-NE0008582. Research presented in this article was also supported by the Laboratory Directed Research and Development (LDRD) program of Los Alamos National Laboratory (LANL). LANL, an affirmative action/equal opportunity employer, is managed by Triad National Security, LLC, for the National Nuclear Security Administration of the U.S. Department of Energy under contract 89233218CNA000001. Portions of this research were also supported by collaboration, services, and infrastructure through the Nuclear Science Center User Facility at (WSU), and the Alexandra Navrotsky Institute for Experimental Thermodynamics. Portions of this research used Beamline 6-ID-C (XSD-SRS) and 11-ID-C (XSD-SRS) of the Advance Photon Source (APS), a U.S. DOE Office of Science User Facility operated for the DOE Office of Science by Argonne National Laboratory (ANL) under Contract No. DE-AC02-06CH11357.

Figures

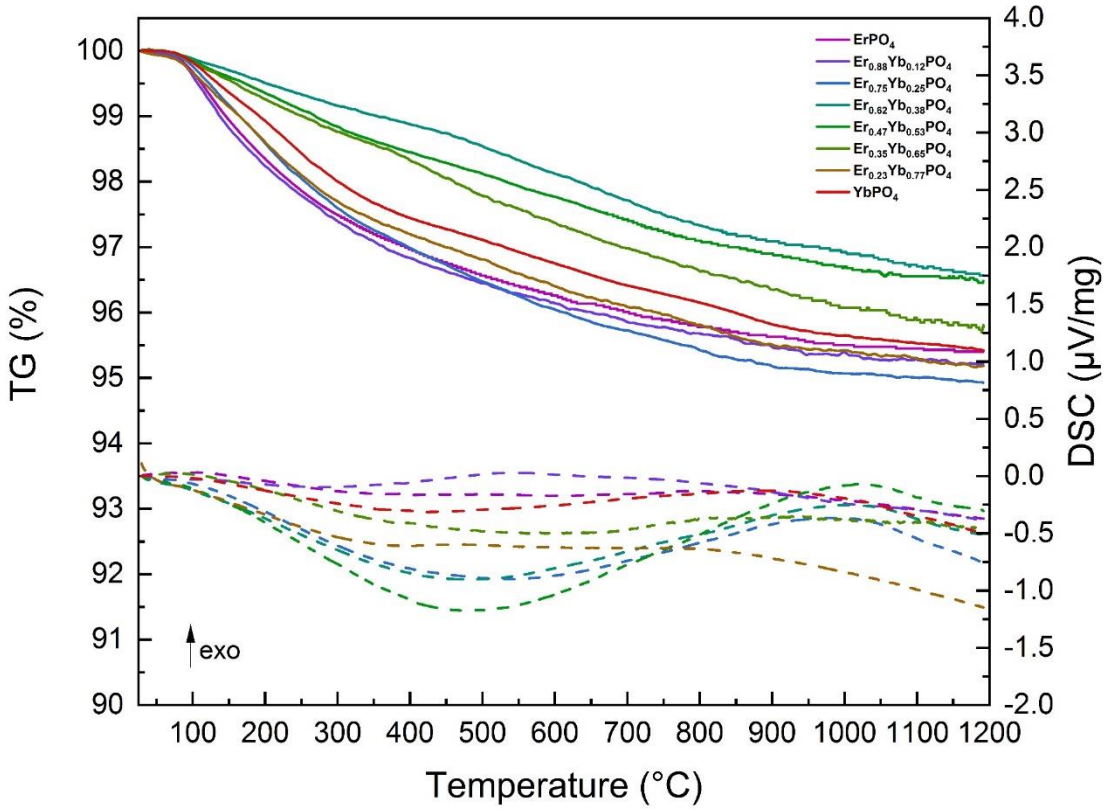

Figure 1: TGA-DSC curves of $Er_{(x)}Yb_{(1-x)}PO_4$ samples, where the TG traces are solid curves and DSC traces are dashed curves.

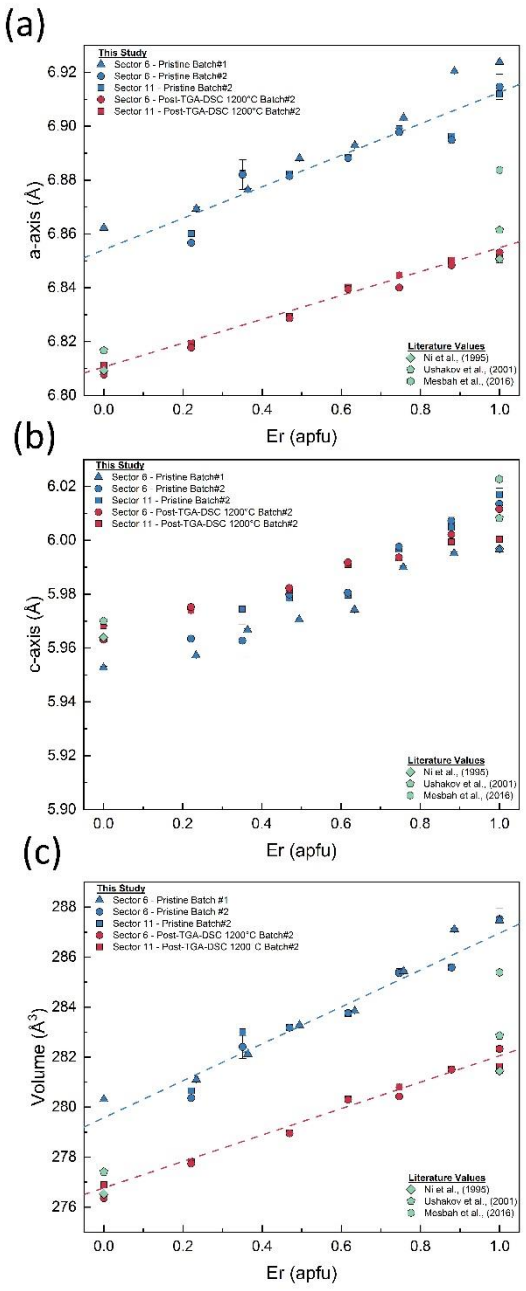

Figure 2: Variation of unit cell parameters of $Er_{(x)}Yb_{(1-x)}PO_4$. *Blue symbols* (a-c) indicate the data points taken on the pristine samples, *red symbols* indicate date collected on the samples recovered after TGA-DSC, *green symbols* indicate literature values.[25,63,69] The data represented with *triangles* are those of the first batch collected at beamline 6 ID-D, *circles* are from the second batch collected at beamline 6 ID-D, and *squares* are second batch collected at beamline 11 ID-D.

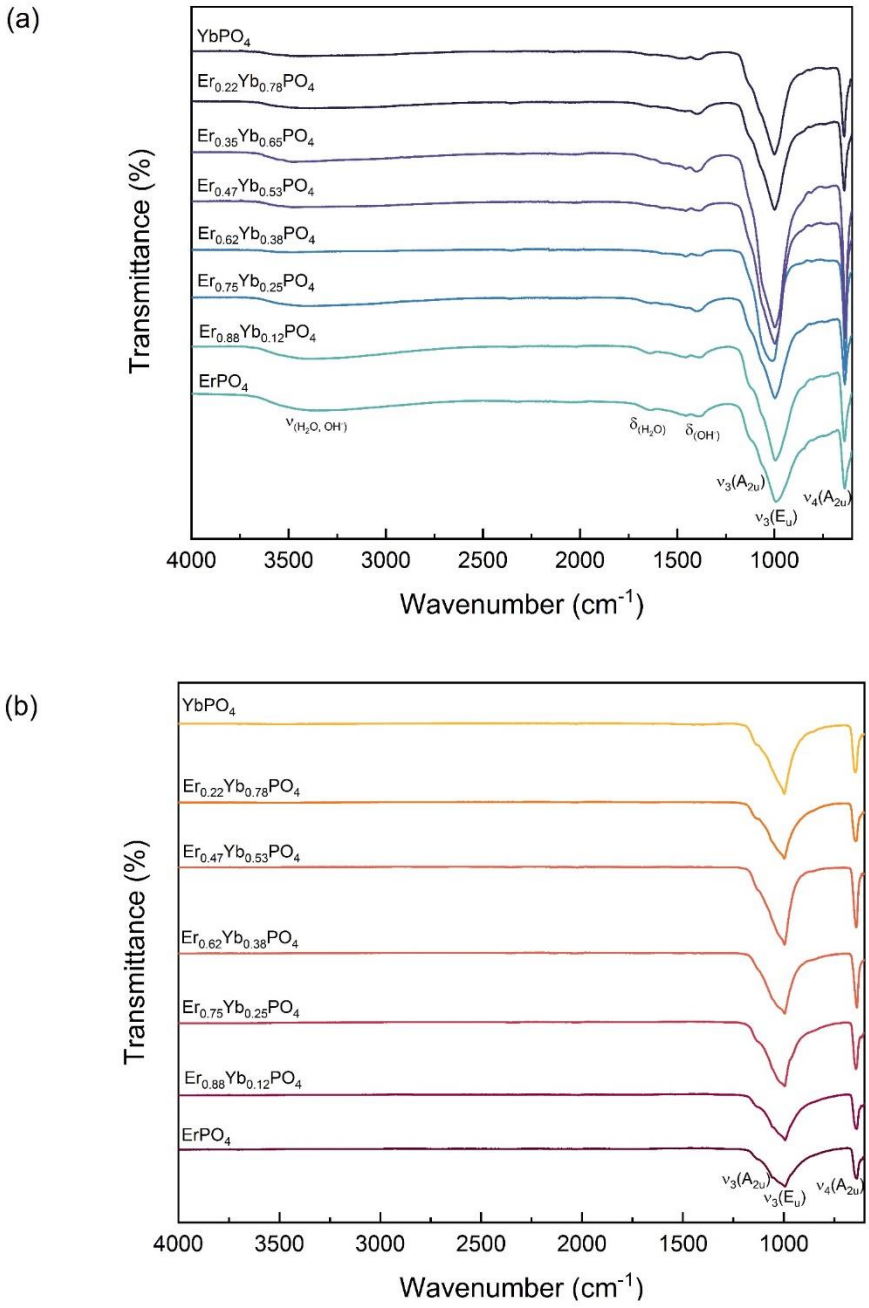

Figure 3: FTIR spectra of (a) pristine $Er_{(x)}Yb_{(1-x)}PO_4$ and (b) $Er_{(x)}Yb_{(1-x)}PO_4$ after the TGA-DSC experiments to 1200 °C.

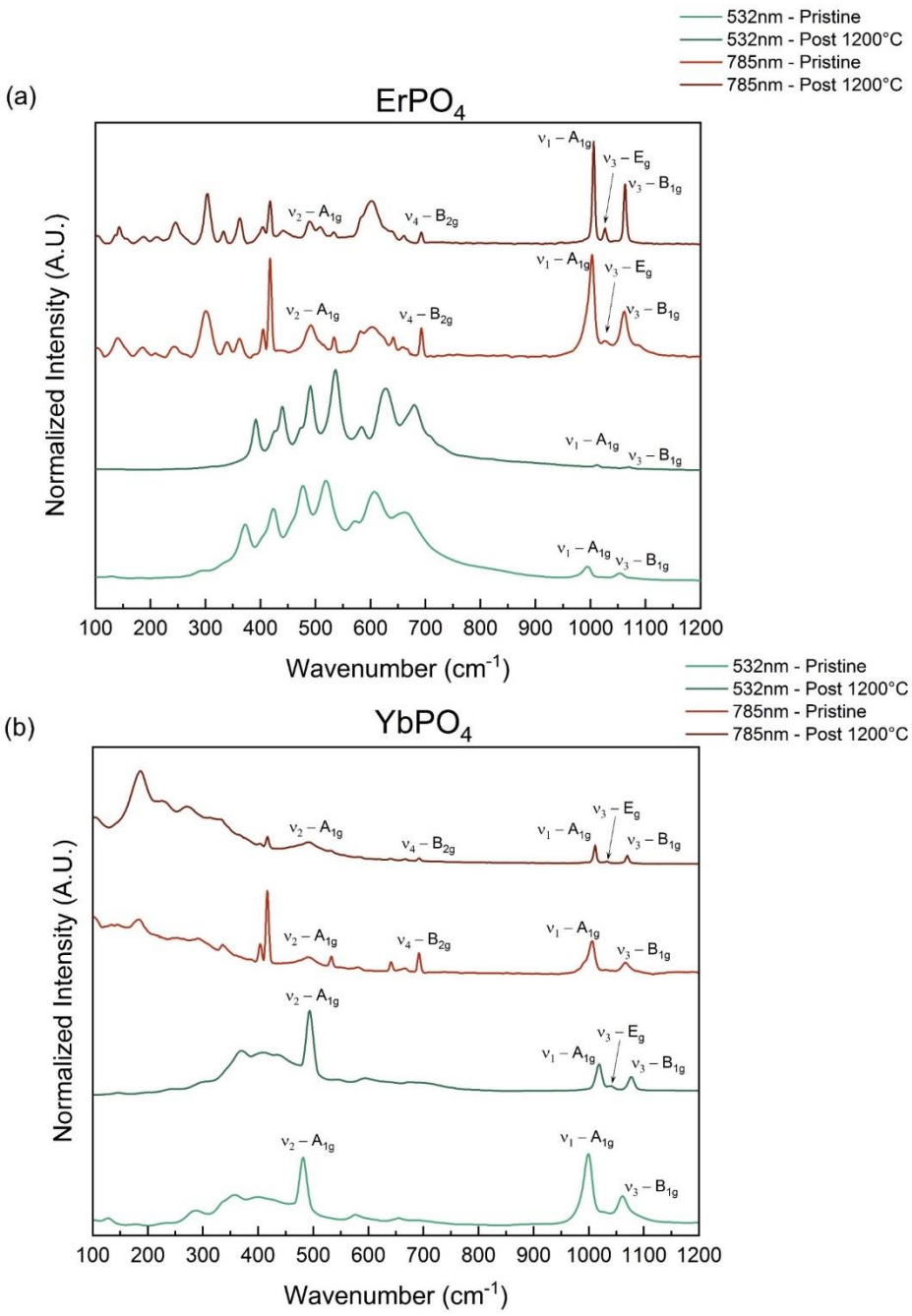

Figure 4: Raman spectra collected with both 532 nm and 785 nm lasers for (a) $ErPO_4$ and (b) $YbPO_4$.

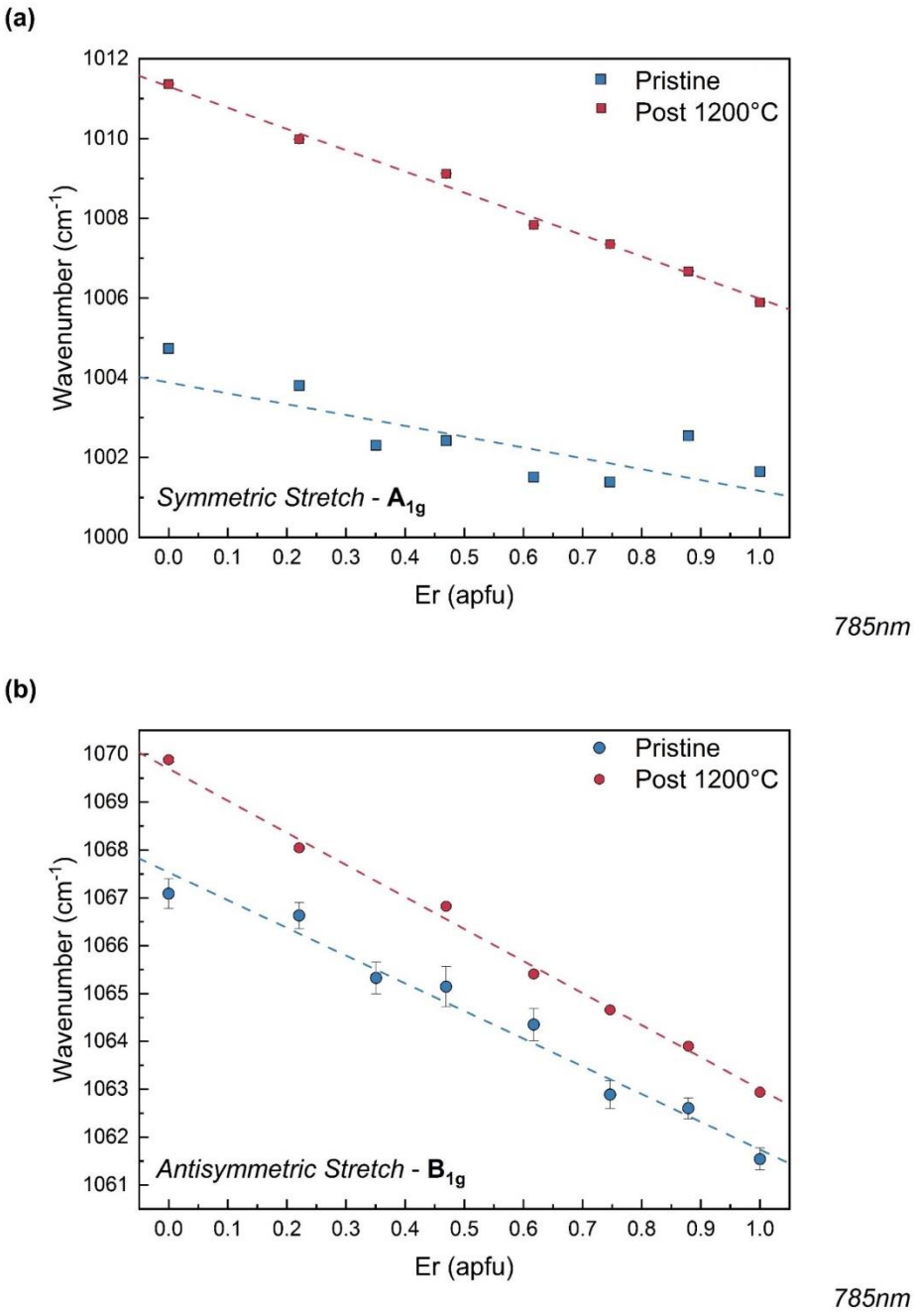

Figure 5: Variation in the P-O stretching motions as a function of Er content.

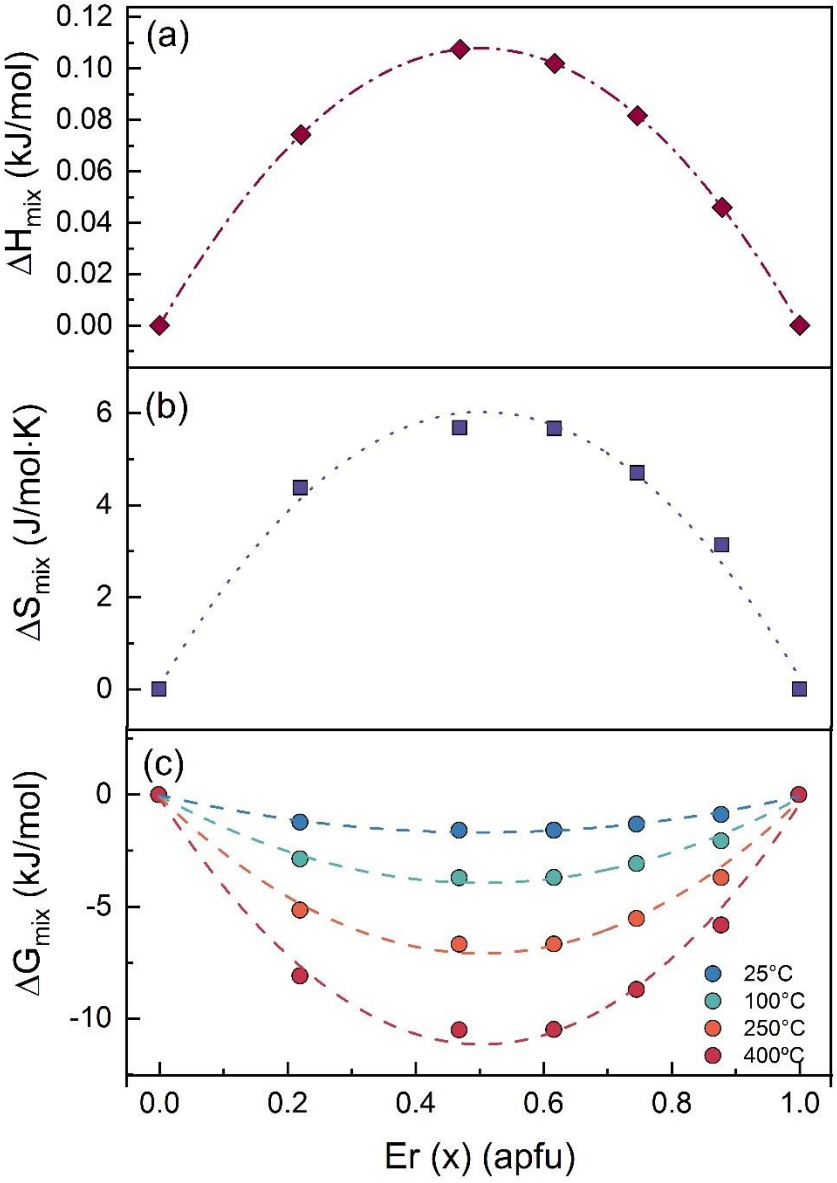

Figure 6: (a) Enthalpies of mixing. (b) Entropies of mixing. (c) Gibbs free energy of mixing.

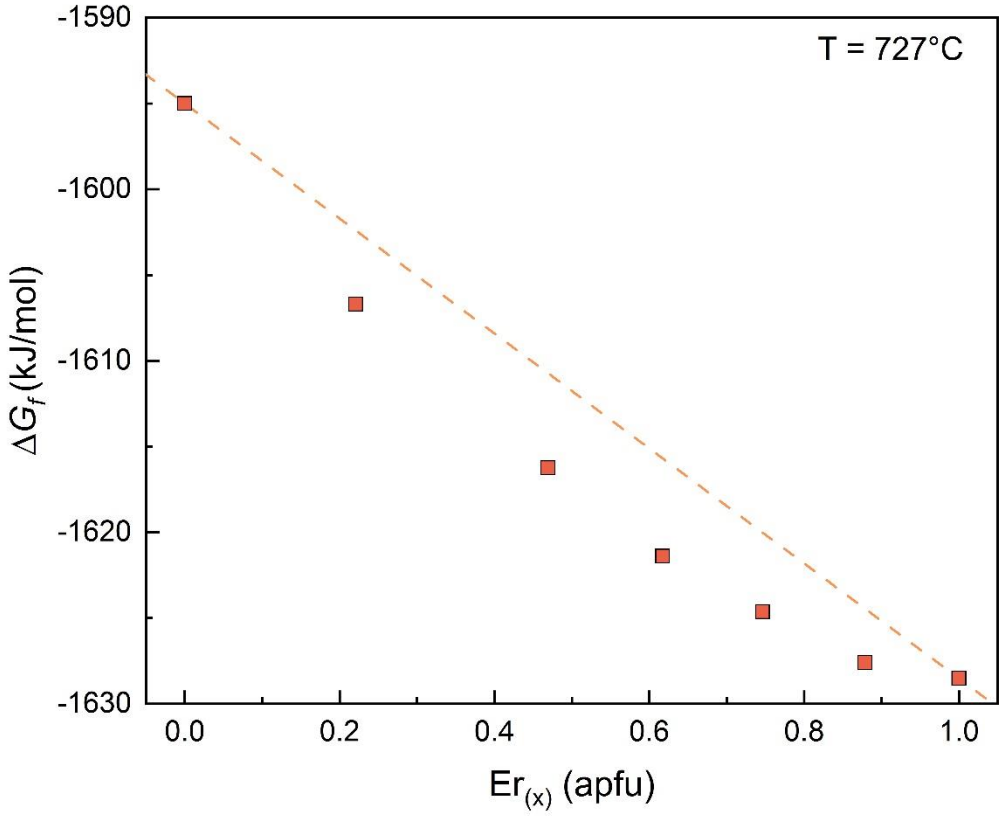

Figure 7: Predicted free energy of formation (ΔG_f) for $Er_{(x)}Yb_{(1-x)}PO_4$ at 727 °C.

References

(1) N. G, Connelly; T., Damhus; R. M., H. A. T. H. *Nomenclature of Inorganic Chemistry IUPAC Recommendations 2005 IUPAC Periodic Table of the Elements Fm No. (2005)*; 2005.

(2) Haxel, G. B.; Hedrick, J. B.; Orris, G. J. Rare Earth Elements — Critical Resources for High Technology. *United States Geol. Surv. Fact Sheet* **2002**, *087*, 4.

(3) Bunzli, J.-C. G.; McGill, I. Rare Earth Elements. In *Ullmann's Encyclopedia of Industrial Chemistry*; 2018

(4) Han, J.; Wang, Y.; Liu, R.; Wan, F. Theoretical and Experimental Investigation of Xenotime-Type Rare Earth Phosphate REPO4, (RE = Lu, Yb, Er, Y and Sc) for Potential Environmental Barrier Coating Applications. *Sci. Rep.* **2020**, *10* (1), 1–13.

(5) Herweyer, L. A.; Opila, E. J. High-Temperature Na2SO4 Interaction with Air Plasma Sprayed Yb2Si2O7 + Si EBC System: Topcoat Behavior. *J. Am. Ceram. Soc.* **2021**.

(6) Ridley, M.; Gaskins, J.; Hopkins, P.; Opila, E. Tailoring Thermal Properties of Multi-Component Rare Earth Monosilicates. *Acta Mater.* **2020**, *195*, 698–707.

(7) Golden, R. A.; Mueller, K.; Opila, E. J. Thermochemical Stability of Y2Si2O7 in High-Temperature Water Vapor. *J. Am. Ceram. Soc.* **2020**, *103* (8), 4517–4535.

(8) Costa, G.; Harder, B. J.; Wiesner, V. L.; Jacobson, N. S.; Zhu, D.; Kapush, D.; Bansal, N.; Lee, K. N.; Ushakov, S. V; Navrotsky, A.; et al. Thermodynamics of Reaction between Gas - Turbine Ceramic Coatings and Ingested CMAS Corrodents. *J. Am. Ceram. Soc.* **2018**, 2948–2964.

(9) Costa, G.; Harder, B. J.; Bansal, N. P.; Kowalski, B. A.; Stokes, J. L. Thermochemistry of Calcium Rare-Earth Silicate Oxyapatites. *J. Am. Ceram. Soc.* **2020**, *103* (2), 1446–1453.

(10) Ayyasamy, M. V.; Deijkers, J. A.; Wadley, H. N. G.; Balachandran, P. V. Density Functional Theory and Machine Learning Guided Search for RE2Si2O7 with Targeted Coefficient of Thermal Expansion. *J. Am. Ceram. Soc.* **2020**, No. January, 1–9.

(11) Lee, K. N.; Fox, D. S.; Bansal, N. P. Rare Earth Silicate Environmental Barrier Coatings

for SiC/SiC Composites and Si3N4 Ceramics. *J. Eur. Ceram. Soc.* **2005**, *25* (10 SPEC. ISS.), 1705–1715.

(12) Xu, Y.; Hu, X.; Xu, F.; Li, K. Rare Earth Silicate Environmental Barrier Coatings: Present Status and Prospective. *Ceram. Int.* **2017**, *43* (8), 5847–5855.

(13) Castor, S.B., Hendrick, J. B. Rare Earth Elements. *Ind. Miner. Rocks Commod. Mark. Uses* **2006**, 769–792.

(14) Dai, S.; Graham, I. T.; Ward, C. R. A Review of Anomalous Rare Earth Elements and Yttrium in Coal. *Int. J. Coal Geol.* **2016**, *159*, 82–95.

(15) Shannon, R. D. Revised Effective Ionic Radii and Systematic Studies of Interatomic Distances in Halides and Chalcogenides. *Acta Crystallogr. Sect. A* **1976**, *32* (5), 751–766.

(16) Kanazawa, Y.; Kamitani, M. Rare Earth Minerals and Resources in the World. *J. Alloys Compd.* **2006**, *408–412*, 1339–1343.

(17) Taggart, R. K.; Hower, J. C.; Dwyer, G. S.; Hsu-Kim, H. Trends in the Rare Earth Element Content of U.S.-Based Coal Combustion Fly Ashes. *Environ. Sci. Technol.* **2016**, *50* (11), 5919–5926.

(18) Williams-Jones, A. E.; Wollenberg, R.; Bodeving, S. Hydrothermal Fractionation of the Rare Earth Elements and the Genesis of the Lofdal REE Deposit, Namibia. In *Symposium on critical and strategic materials. British Columbia Geological Survey Paper*; 2015; pp 125–130.

(19) Richter, L.; Diamond, L. W.; Atanasova, P.; Banks, D. A.; Gutzmer, J. Hydrothermal Formation of Heavy Rare Earth Element (HREE)- Xenotime Deposits at 100 °C in a Sedimentary Basin. *Geology* **2018**, *46* (3), 263–266.

(20) Li, M. Y. H.; Zhou, M. F.; Williams-Jones, A. E. The Genesis of Regolith-Hosted Heavy Rare Earth Element Deposits: Insights from the World-Class Zudong Deposit in Jiangxi Province, South China. *Econ. Geol.* **2019**, *114* (3), 541–568.

(21) Cook, N. J.; Ciobanu, C. L.; O'Rielly, D.; Wilson, R.; Das, K.; Wade, B. Mineral Chemistry of Rare Earth Element (REE) Mineralization, Browns Ranges, Western

Australia. *Lithos* **2013**, *172–173*, 192–213.

(22) Gysi, A. P.; Van Hoozen, C.; Harlov, D. Hydrothermal Solubility of TbPO4, HoPO4, TmPO4, and LuPO4 Xenotime Endmembers at PH of 2 and Temperatures between 100 and 250 °C. *Chem. Geol.* **2021**, *567* (January), 120072.

(23) Navrotsky, A.; Lee, W.; Mielewczyk-Gryn, A.; Ushakov, S. V.; Anderko, A.; Wu, H.; Riman, R. E. Thermodynamics of Solid Phases Containing Rare Earth Oxides. *J. Chem. Thermodyn.* **2015**, *88*, 126–141.

(24) Gysi, A. P.; Harlov, D.; Filho, D. C.; Williams-Jones, A. E. Experimental Determination of the High Temperature Heat Capacity of a Natural Xenotime-(Y) Solid Solution and Synthetic DyPO4 and ErPO4 Endmembers. *Thermochim. Acta* **2016**, *627–629*, 61–67.

(25) Ushakov, S. V.; Helean, K. B.; Navrotsky, A.; Boatner, L. A. Thermochemistry of Rare-Earth Orthophosphates. *J. Mater. Res.* **2001**, *16* (9), 2623–2633.

(26) Gysi, A. P.; Williams-Jones, A. E.; Harlov, D. The Solubility of Xenotime-(Y) and Other HREE Phosphates (DyPO4, ErPO4 and YbPO4) in Aqueous Solutions from 100 to 250°C and Psat. *Chem. Geol.* **2015**, *401*, 83–95.

(27) Lacomba-Perales, R.; Errandonea, D.; Meng, Y.; Bettinelli, M. High-Pressure Stability and Compressibility of A PO4 (A=La, Nd, Eu, Gd, Er, and Y) Orthophosphates: An x-Ray Diffraction Study Using Synchrotron Radiation. *Phys. Rev. B - Condens. Matter Mater. Phys.* **2010**, *81* (6), 1–9.

(28) Zhang, F. X.; Lang, M.; Ewing, R. C.; Lian, J.; Wang, Z. W.; Hu, J.; Boatner, L. A. Pressure-Induced Zircon-Type to Scheelite-Type Phase Transitions in YbPO4 and LuPO4. *J. Solid State Chem.* **2008**, *181* (10), 2633–2638.

(29) Gomis, O.; Lavina, B.; Rodríguez-Hernández, P.; Muñoz, A.; Errandonea, R.; Errandonea, D.; Bettinelli, M. High-Pressure Structural, Elastic, and Thermodynamic Properties of Zircon-Type HoPO4 and TmPO4. *J. Phys. Condens. Matter* **2017**, *29* (9).

(30) López-Solano, J.; Rodríguez-Hernández, P.; Muñoz, A.; Gomis, O.; Santamaría-Perez, D.; Errandonea, D.; Manjón, F. J.; Kumar, R. S.; Stavrou, E.; Raptis, C. Theoretical and Experimental Study of the Structural Stability of TbPO 4 at High Pressures. *Phys. Rev. B -*

Condens. Matter Mater. Phys. **2010**, *81* (14), 1–9.

(31) Migdisov, A.; Guo, X.; Nisbet, H.; Xu, H.; Williams-Jones, A. E. Fractionation of REE, U, and Th in Natural Ore-Forming Hydrothermal Systems: Thermodynamic Modeling. *J. Chem. Thermodyn.* **2019**, *128*, 305–319.

(32) Anderson, G. M.; Crerar, D. A. *Thermodynamics in Geochemistry: The Equilibrium Model*; Oxford University Press: New York, 1993.

(33) Konings, R. J. M.; Walter, M.; Popa, K. Excess Properties of the (Ln2-2xCaxThx)(PO4)2 (Ln = La, Ce) Solid Solutions. *J. Chem. Thermodyn.* **2008**, *40* (8), 1305–1308.

(34) Popa, K.; Konings, R. J. M.; Geisler, T. High-Temperature Calorimetry of (La1-XLnx)PO4 Solid Solutions. *J. Chem. Thermodyn.* **2007**, *39* (2), 236–239.

(35) Popa, K.; Sedmidubský, D.; Beneš, O.; Thiriet, C.; Konings, R. J. M. The High-Temperature Heat Capacity of LnPO4 (Ln = La, Ce, Gd) by Drop Calorimetry. *J. Chem. Thermodyn.* **2006**, *38* (7), 825–829.

(36) Ji, Y.; Kowalski, P. M.; Kegler, P.; Huittinen, N.; Marks, N. A.; Vinograd, V. L.; Arinicheva, Y.; Neumeier, S.; Bosbach, D. Rare-Earth Orthophosphates From Atomistic Simulations. *Front. Chem.* **2019**, *7* (April), 1–12.

(37) Mogilevsky, P. On the Miscibility Gap in Monazite-Xenotime Systems. *Phys. Chem. Miner.* **2007**, *34* (3), 201–214.

(38) Hikichi, Y.; Nomura, T. Melting Temperatures of Monazite and Xenotime. *J. Am. Ceram. Soc.* **1987**, *70* (10), C-252-C-253.

(39) Gavrichev, K. S.; Smirnova, N. N.; Gurevich, V. M.; Danilov, V. P.; Tyurin, A. V.; Ryumin, M. A.; Komissarova, L. N. Heat Capacity and Thermodynamic Functions of LuPO4 in the Range 0-320 K. *Thermochim. Acta* **2006**, *448* (1), 63–65.

(40) Tyurin, A. V.; Ryumin, M. A.; Khoroshilov, A. V.; Gurevich, V. M.; Gavrichev, K. S. Thermodynamic Functions of Holmium Orthophosphate HoPO4 in the Range 9–1370 K. *Thermochim. Acta* **2020**, *683*, 178459.

(41) Gavrichev, K. S.; Ryumin, M. A.; Tyurin, A. V.; Gurevich, V. M.; Nikiforova, G. E.;

Komissarova, L. N. Heat Capacity and Thermodynamic Functions of YbPO4 from 0 to 1800 K. *Inorg. Mater.* **2013**, *49* (7), 701–708.

(42) Gavrichev, K. S.; Ryumin, M. A.; Tyurin, A. V.; Gurevich, V. M.; Khoroshilov, A. V.; Komissarova, L. N. Thermodynamic Functions of Erbium Orthophosphate ErPO 4 in the Temperature Range of 0-1600 K. *Thermochim. Acta* **2012**, *535*, 1–7.

(43) Gavrichev, K. S.; Ryumin, M. A.; Tyurin, A. V.; Gurevich, V. M.; Komissarova, L. N. Heat Capacity and Thermodynamic Functions of Xenotime YPO4(c) at 0-1600 K. *Geochemistry Int.* **2010**, *48* (9), 932–939.

(44) Goncharov, V. G.; Nisbet, H. D.; Strzelecki, A. C.; Benmore, C. J.; Migdisov, A. A.; Xu, H.; Guo, X. Energetics of Hydroxylbastnäsite Solid Solutions, La1-XNdxCO3OH. *Geochim. Cosmochim. Acta2* **2022**, *Submitted*.

(45) Ewing, R. C.; Wang, L. M. Phosphates as Nuclear Waste Forms. In *Phosphates: Geochemical, Geobiological and Materials Importance*; Kohn, M. J., Rakovan, J., Hughes, J. M., Eds.; Mineralogical Society of America, 2002; Vol. 48, pp 673–700.

(46) Boatner, L. A. Synthesis, Structure, and Properties of Monazite, Pretulite, and Xenotime. In *Reviews in Mineralogy and Geochemistry*; 2002; Vol. 48, pp 87–121.

(47) Orlova, A. I.; Ojovan, M. I. Ceramic Mineral Waste-Forms for Nuclear Waste Immobilization. *Materials (Basel).* **2019**, *12* (16), 2638.

(48) Rafiuddin, M. R.; Grosvenor, A. P. Probing the Effect of Radiation Damage on the Structure of Rare-Earth Phosphates. *J. Alloys Compd.* **2015**, *653*, 279–289.

(49) Boatner, L. A.; Abraham, M. M.; Sales, B. C. Lanthanide Orthophosphate Ceramics for the Disposal of Actinide-Contaminated Nuclear Wastes. *Inorganica Chim. Acta* **1984**, *94* (1–3), 146–148.

(50) Lumpkin, G. R. Ceramic Waste Forms for Actinides. *Elements* **2006**, *2* (6), 365–372.

(51) Vance, E. R.; Zhang, Y.; McLeod, T.; Davis, J. Actinide Valences in Xenotime and Monazite. *J. Nucl. Mater.* **2011**, *409* (3), 221–224.

(52) Cotton, S. *Lanthanide and Actinide Chemistry*; John Wiley & Sons, Ltd, 2006.

(53) Morss, L. R.; Edelstein, N. M.; Fuger, J. *The Chemistry of the Actinides and Transactinide Elements*, Fourth.; Morss, L. R., Edelstein, N. M., Fuger, J., Eds.; Springer: Dordrecht, 2010.

(54) Strzelecki, A. C.; Bourgeois, C.; Kriegsman, K. W.; Estevenon, P.; Wei, N.; Szenknect, S.; Mesbah, A.; Wu, D.; Ewing, R. C.; Dacheux, N.; et al. Thermodynamics of CeSiO4 : Implications for Actinide Orthosilicates. *Inorg. Chem.* **2020**, *59* (18), 13174–13183.

(55) Guo, X.; Szenknect, S.; Mesbah, A.; Labs, S.; Clavier, N.; Poinssot, C.; Ushakov, S. V.; Curtius, H.; Bosbach, D.; Ewing, R. C.; et al. Thermodynamics of Formation of Coffinite, USiO4. *Proc. Natl. Acad. Sci.* **2015**, *112* (21), 6551–6555.

(56) Guo, X.; Szenknect, S.; Mesbah, A.; Clavier, N.; Poinssot, C.; Wu, D.; Xu, H.; Dacheux, N.; Ewing, R. C.; Navrotsky, A. Energetics of a Uranothorite (Th1-XUxSiO4) Solid Solution. *Chem. Mater.* **2016**, *28* (19), 7117–7124.

(57) Hobart, D. E.; Begun, G. M.; Haire, R. G.; Hellwege, H. E. Raman Spectra of the Transplutonium Orthophosphates and Trimetaphosphates. *J. Raman Spectrosc.* **1983**, *14* (1), 59–62.

(58) Popa, K.; Vigier, J. F.; Martel, L.; Manara, D.; Colle, J. Y.; Blanco, O. D.; Wiss, T.; Freis, D.; Konings, R. J. M. Synthesis, Characterization, and Stability of Americium Phosphate, AmPO4. *Inorg. Chem.* **2020**, *59* (9), 6595–6602.

(59) Bjorklund, C. W. The Preparation of PuP2O7 and PuPO4. *Phys. Inorg. Chem.* **1958**, *19* (24), 6347–6350.

(60) Begg, B. D.; Vance, E. R.; Conradson, S. D. The Incorporation of Plutonium and Neptunium in Zirconolite and Perovskite. *J. Alloys Compd.* **1998**, *271–273*, 221–226. https://doi.org/10.1016/S0925-8388(98)00058-9.

(61) Szenknect, S.; Costin, D. T.; Clavier, N.; Mesbah, A.; Poinssot, C.; Vitorge, P.; Dacheux, N. From Uranothorites to Coffinite: A Solid Solution Route to the Thermodynamic Properties of USiO4. *Inorg. Chem.* **2013**, *52* (12), 6957–6968.

(62) Marcial, J.; Zhang, Y.; Zhao, X.; Xu, H.; Mesbah, A.; Nienhuis, E. T.; Szenknect, S.; Lin, J.; Qi, L.; Migdisov, A. A.; et al. Thermodynamic Non-Ideality and Disorder

Heterogeneity in Actinide Silicate Solid Solutions. *Mater. Degrad.* **2021**, *5* (34), 1–14.

(63) Mesbah, A.; Clavier, N.; Lozano-Rodriguez, M. J.; Szenknect, S.; Dacheux, N. Incorporation of Thorium in the Zircon Structure Type through the Th1-XErx(SiO4)1-x(PO4)x Thorite-Xenotime Solid Solution. *Inorg. Chem.* **2016**, *55* (21), 11273–11282.

(64) Bruker Nano GmbH. S2 Picofox™. Bruker Nano GmbH: Berlin 2010.

(65) Bruker Nano GmbH. Spectra 7. Bruker Nano GmbH: Berlin 2010.

(66) Prescher, C.; Prakapenka, V. B. DIOPTAS: A Program for Reduction of Two-Dimensional X-Ray Diffraction Data and Data Exploration. *High Press. Res.* **2015**, *35* (3), 223–230.

(67) Strzelecki, A. C.; Barral, T.; Estevenon, P.; Mesbah, A.; Goncharov, V.; Baker, J.; Bai, J.; Clavier, N.; Szenknect, S.; Migdisov, A.; et al. The Role of Water and Hydroxyl Groups in the Structures of Stetindite and Coffinite, MSiO4 (M = Ce, U). *Inorg. Chem.* **2021**.

(68) Toby, B. H.; Von Dreele, R. B. GSAS-II: The Genesis of a Modern Open-Source All Purpose Crystallography Software Package. *J. Appl. Crystallogr.* **2013**, *46* (2), 544–549.

(69) Ni, Y.; Hughes, J. M.; Mariano, A. N. Crystal Chemistry of the Monazite and Xenotime Structures. *Am. Mineral.* **1995**, *80* (1–2), 21–26.

(70) Estevenon, P.; Welcomme, E.; Szenknect, S.; Mesbah, A.; Moisy, P.; Poinssot, C.; Dacheux, N. Preparation of CeSiO 4 from Aqueous Precursors under Soft Hydrothermal Conditions . *Dalt. Trans.* **2019**, *48* (22), 7551–7559.

(71) Estevenon, P.; Kaczmarek, T.; Vadot, F.; Dumas, T.; Solari, P. L.; Welcomme, E.; Szenknect, S.; Mesbah, A.; Moisy, P.; Poinssot, C.; et al. Formation of CeSiO4 from Cerium (III) Silicate Precursors. *Dalt. Trans.* **2019**, *48*, 10455–10463.

(72) Estevenon, P.; Kaczmarek, T.; Rafiuddin, M. R.; Welcomme, E.; Szenknect, S.; Mesbah, A.; Moisy, P.; Poinssot, C.; Dacheux, N. Soft Hydrothermal Synthesis of Hafnon, HfSiO 4 . *Cryst. Growth Des.* **2020**.

(73) Estevenon, P.; Welcomme, E.; Tamain, C.; Jouan, G.; Szenknect, S.; Mesbah, A.; Poinssot, C.; Moisy, P.; Dacheux, N. Formation of PuSiO4 under Hydrothermal

Conditions. *Dalt. Trans.* **2020**.

(74) Estevenon, P.; Welcomme, E.; Szenknect, S.; Mesbah, A.; Moisy, P.; Poinssot, C.; Dacheux, N. Multiparametric Study of the Synthesis of ThSiO 4 under Hydrothermal Conditions. *Inorg. Chem.* **2018**, *57* (15), 9393–9402.

(75) Estevenon, P.; Dumas, T.; Solari, P. L.; Welcomme, E.; Szenknect, S.; Mesbah, A.; Kvashnina, K. O.; Moisy, P.; Poinssot, C.; Dacheux, N. Formation of Plutonium(Iv) Silicate Species in Very Alkaline Reactive Media . *Dalt. Trans.* **2021**.

(76) Pavlik, A.; Ushakov, S. V.; Navrotsky, A.; Benmore, C. J.; Weber, R. J. K. Structure and Thermal Expansion of Lu2O3 and Yb2O3 up to the Melting Points. *J. Nucl. Mater.* **2017**, *495*, 385–391.

(77) Clavier, N.; Szenknect, S.; Costin, D. T.; Mesbah, A.; Ravaux, J.; Poinssot, C.; Dacheux, N. Purification of Uranothorite Solid Solutions from Polyphase Systems. *J. Nucl. Mater.* **2013**, *441* (1–3), 73–83.

(78) Dawson, P.; Hargreave, M. M.; Wilkinson, G. R. The Vibrational Spectrum of Zircon (ZrSiO4). *J. Phys. C Solid State Phys.* **1971**, *4* (2), 240–256.

(79) Clavier, N.; Szenknect, S.; Costin, D. T.; Mesbah, A.; Poinssot, C.; Dacheux, N. From Thorite to Coffinite: A Spectroscopic Study of Th1-XUxSiO4 Solid Solutions. *Spectrochim. Acta - Part A Mol. Biomol. Spectrosc.* **2014**, *118*, 302–307.

(80) Clavier, N.; Mesbah, A.; Szenknect, S.; Dacheux, N. Monazite, Rhabdophane, Xenotime & Churchite: Vibrational Spectroscopy of Gadolinium Phosphate Polymorphs. *Spectrochim. Acta - Part A Mol. Biomol. Spectrosc.* **2018**, *205*, 85–94.

(81) Nasdala, L.; Zhang, M.; Kempe, U.; Panczer, G.; Gaft, M.; Andrut, M.; Plötze, M. Spectroscopic Methods Applied to Zircon. In *Reviews in Mineralogy and Geochemistry: Zircon*; 2003; pp 427–467.

(82) Nasdala, L.; Beran, A.; Libowitzky, E.; Wolf, D. The Incorporation of Hydroxyl Groups and Molecular Water in Natural Zircon (ZrSiO4). *Am. J. Sci.* **2001**, *301* (10), 831–857.

(83) Abe, T.; Kuribayashi, T.; Nakamura, M. OH Defects in Synthetic Xenotime (YPO4). *Eur.*

J. Mineral. **2016**, *28* (3), 641–648.

(84) Kolesov, B. A.; Geiger, C. A.; Armbruster, T. The Dynamic Properties of Zircon Studied by Single-Crystal X-Ray Diffraction and Raman Spectroscopy. *Eur. J. Mineral.* **2001**, *13* (5), 939–948.

(85) Hoskin, P. W. O.; Rodgers, K. A. Raman Spectral Shift in the Isomorphous (Zr1-XHfx)SiO4. *Eur. J. solid state Inorg. Chem.* **1996**, *33* (11), 1111–1121.

(86) Syme, R. W. G.; Lockwood, D. J.; Kerr, H. J. Raman Spectrum of Synthetic Zircon (ZrSiO 4) and Raman Spectrum of Synthetic Zircon (ZrSiO ,) and Thorite. *Solid State Phys.* **1977**, *10*, 1335–1348.

(87) Begun, G. M.; Beall, G. W.; Boatner, L. A.; Gregor, W. J. Raman Spectra of the Rare Earth Orthophosphates. *J. Raman Spectrosc.* **1982**, *11* (4), 273–278.

(88) Caruba, R.; Baumer, A.; Ganteaume, M.; Iacconi, P. An Experimental Study of Hydroxyl Groups and Water in Synthetic and Natural Zircons: A Model of the Metamict State. *Am. Mineral.* **1985**, *70* (11–12), 1224–1231.

(89) Janeczek, J. Composition and Origin of Coffinite from Jachymov, Czechoslovakia. *Neues Jahrb. für Mineral. Monatshefte* **1991**, *9*, 385–395.

(90) Kijkowska, R. Thermal Decomposition of Lanthanide Orthophosphates Synthesized through Crystallisation from Phosphoric Acid Solution. *Thermochim. Acta* **2003**, *404* (1–2), 81–88.

(91) Taylor, S. R.; Mclennan, S. M. The Geochemical Evolution of the Continental Crust. *Am. Geophys. Union* **1995**, *33* (2), 241–265.

(92) Xu, H.; Navrotsky, A.; Su, Y.; Balmer, M. Lou. Perovskite Solid Solutions along the NaNbO 3-SrTiO 3 Join: Phase Transitions, Formation Enthalpies, and Implications for General Perovskite Energetics. *Chem. Mater.* **2005**, *17* (7), 1880–1886.

(93) Xu, H.; Su, Y.; Balmer, M. Lou; Navrotsky, A. A New Series of Oxygen-Deficient Perovskites in the NaTixNb1-XO3-0.5x System: Synthesis, Crystal Chemistry, and Energetics. *Chem. Mater.* **2003**, *15* (9), 1872–1878.

(94) Xu, H.; Navrotsky, A.; Balmer, M. Lou; Su, Y.; Bitten, E. R. Energetics of Substituted Pollucites Along the CsAlSi2O6–CsTiSi2O6.5 Join : A High-Temperature Calorimetric Study. *J. Am. Ceram. Soc.* **2001**, *84* (3), 555–560.

(95) Xu, H.; Navrotsky, A.; Nyman, M. D.; Nenoff, T. M. Octahedral Microporous Phases Na2Nb2-x TixO6-x (OH)X·H2O and Their Related Perovskites: Crystal Chemistry, Energetics, and Stability Relations. *J. Mater. Res.* **2005**, *20* (3), 618–627.

(96) Hirsch, A.; Kegler, P.; Alencar, I.; Ruiz-Fuertes, J.; Shelyug, A.; Peters, L.; Schreinemachers, C.; Neumann, A.; Neumeier, S.; Liermann, H. P.; et al. Structural, Vibrational, and Thermochemical Properties of the Monazite-Type Solid Solution La1–XPrxPO4. *J. Solid State Chem.* **2017**, *245* (August 2016), 82–88.

(97) Schlenz, H.; Dellen, J.; Kegler, P.; Gatzen, C.; Schreinemachers, C.; Shelyug, A.; Klinkenberg, M.; Navrotsky, A.; Bosbach, D. Structural and Thermodynamic Mixing Properties of La1-XNdxPO4 Monazite-Type Solid Solutions. *J. Solid State Chem.* **2019**, *270*, 470–478.

(98) Glynn, P. Solid-Solution Solubilities and Thermodynamics: Sulfates, Carbonates and Halides. *Sulfate Miner. Crystallogr. Geochemistry, Environ. Significance* **2000**, *40*, 481–511.

(99) Jenkins, H. D. B.; Glasser, L. Standard Absolute Entropy, S298o, Values from Volume or Density. *Inorg. Chem.* **2003**, *42* (26), 8702–8708.

(100) Glasser, L. Thermodynamics of Condensed Phases: Formula Unit Volume, Vm, and the Determination of the Number of Formula Units, Z, in a Crystallographic Unit Cell. *J. Chem. Educ.* **2011**, *88* (5), 581–585.

(101) Strzelecki, A. C.; Kriegsman, K. W.; Estevenon, P.; Goncharov, V.; Bai, J.; Szenknect, S.; Mesbah, A.; Wu, D.; McCloy, J. S.; Dacheux, N.; et al. High-Temperature Thermodynamics of Cerium Silicates, A-Ce2Si2O7 and Ce4.67(SiO4)3O. *ACS Earth Sp. Chem.* **2020**, *4* (11), 2129–2143.

(102) Strzelecki, A. C.; Ren, Y.; Chong, S.; Riley, B. J.; Xu, H.; McCloy, J. S.; Guo, X. Structure and Thermodynamics of Calcium Rare Earth Silicate Oxyapatites,

Ca2RE8(SiO4)6O2 (RE = Pr, Tb, Ho, Tm). *Phys. Chem. Miner.* **2021**, *Pending Re*.

(103) Guo, X.; Xu, H. Enthalpies of Formation of Polyhalite: A Mineral Relevant to Salt Repository. *J. Chem. Thermodyn.* **2017**, *114*, 44–47.

(104) Robie, Richard A.;Hemingway, B. S. Thermodynamic Properties of Minerals and Related Substances at 298.15 K and 1 Bar (105 Pascals) Pressure and at Higher Temperatures. *U.S. Geol. Surv. Bull.* **1995**, *2131*.

(105) Migdisov, A.; Williams-Jones, A. E.; Brugger, J.; Caporuscio, F. A. Hydrothermal Transport, Deposition, and Fractionation of the REE: Experimental Data and Thermodynamic Calculations. *Chem. Geol.* **2016**, *439* (July 2016), 13–42.

(106) Van Hoozen, C. J.; Gysi, A. P.; Harlov, D. E. The Solubility of Monazite (LaPO4, PrPO4, NdPO4, and EuPO4) Endmembers in Aqueous Solutions from 100 to 250 °C. *Geochim. Cosmochim. Acta* **2020**, *280*, 302–316.

(107) Banks, D. A.; Yardley, B. W. D.; Campbell, A. R.; Jarvis, K. E. REE Composition of an Aqueous Magmatic Fluid: A Fluid Inclusion Study from the Capitan Pluton, New Mexico, U.S.A. *Chem. Geol.* **1994**, *113* (3–4), 259–272.

(108) Smith, M. P.; Henderson, P.; Campbell, L. S. Fractionation of the REE during Hydrothermal Processes: Constraints from the Bayan Obo Fe-REE-Nb Deposit, Inner Mongolia, China. *Geochim. Cosmochim. Acta* **2000**, *64* (18), 3141–3160.

(109) Williams-Jones, A. E.; Samson, I. M.; Olivo, G. R. The Genesis of Hydrothermal Fluorite-REE Deposits in the Gallinas Mountains, New Mexico. *Econ. Geol.* **2000**, *95* (2), 327–341.

(110) Lehmann, B.; Nakai, S.; Höhndorf, A.; Brinckmann, J.; Dulski, P.; Hein, U. F.; Masuda, A. REE Mineralization at Gakara, Burundi: Evidence for Anomalous Upper Mantle in the Western Rift Valley. *Geochim. Cosmochim. Acta* **1994**, *58* (2), 985–992.

(111) Leitner, J.; Sedmidubsky, D.; Ruzicka, K.; Svobo, P. Calorimetric Determination of Heat Capacity, Entropy and Enthalpy of Mixed Oxides in the System CaO–SrO–Bi2O3–Nb2O5–Ta2O5. In *Applications of Calorimetry in a Wide Context - Differential Scanning Calorimetry, Isothermal Titration Calorimetry and Microcalorimetry*; Elkordy, A. A.,

Ed.; BoD – Books on Demand, 2013; pp 385–406.

(112) Konings, R. J. M.; Beneš, O.; Kovács, A.; Manara, D.; Sedmidubskỳ, D.; Gorokhov, L.; Iorish, V. S.; Yungman, V.; Shenyavskaya, E.; Osina, E. The Thermodynamic Properties of the F-Elements and Their Compounds: Part 2. The Lanthanide and Actinide Oxides. *J. Phys. Chem. Ref. Data* **2014**, *43* (1).

(113) Zhao, Z.; Chen, H.; Xiang, H.; Dai, F. Z.; Wang, X.; Peng, Z.; Zhou, Y. (La0.2Ce0.2Nd0.2Sm0.2Eu0.2)PO4: A High-Entropy Rare-Earth Phosphate Monazite Ceramic with Low Thermal Conductivity and Good Compatibility with Al2O3. *J. Mater. Sci. Technol.* **2019**, *35* (12), 2892–2896.

(114) Navrotsky, A. *Physics and Chemistry of Earth Materials*; Cambridge University Press, 1994.

(115) McCormack, S. J.; Navrotsky, A. Thermodynamics of High Entropy Oxides. *Acta Mater.* **2021**, *202*, 1–21.

(116) George, E. P.; Raabe, D.; Ritchie, R. O. High-Entropy Alloys. *Nat. Rev. Mater.* **2019**, *4* (8), 515–534.